NGA-Inspired Nanorobots-Assisted Detection of Multifocal Cancer

Shaolong Shi⬤, *Student Member, IEEE*, Yifan Chen⬤, *Senior Member, IEEE*, and Xin Yao, *Fellow, IEEE*

Abstract—We propose a new framework of computing-inspired multifocal cancer detection procedure (MCDP). Under the rubric of MCDP, the tumor foci to be detected are regarded as solutions of the objective function, the tissue region around the cancer areas represents the parameter space, and the nanorobots loaded with contrast medium molecules for cancer detection correspond to the optimization agents. The process that the nanorobots detect tumors by swimming in the high-risk tissue region can be regarded as the process that the agents search for the solutions of an objective function in the parameter space with some constraints. For multimodal optimization (MMO) aiming to locate multiple optimal solutions in a single simulation run, the niche technology has been widely used. Specifically, the niche genetic algorithm (NGA) has been shown to be particularly effective in solving MMO. It can be used to identify the global optima of multiple hump functions in a running, effectively keep the diversity of the population, and prematurely avoid the genetic algorithm. Learning from the optimization procedure of NGA, we propose the NGA-inspired MCDP in order to locate the tumor targets efficiently while taking into account realistic *in vivo* propagation and controlling of nanorobots, which is different from the use scenario of the standard NGA. To improve the performance of the MCDP, we also modify the crossover operator of the original NGA from crossing within a population to crossing between two populations. Finally, we present comprehensive numerical examples to demonstrate the effectiveness of the NGA-inspired MCDP when the biological objective function is associated with the blood flow velocity profile caused by tumor-induced angiogenesis.

Index Terms—Cancer detection, computing-inspired biodetection, contrast-enhanced medical imaging, multimodal optimization (MMO), nanorobots, niche genetic algorithm (NGA).

Shaolong Shi is with the School of Life Science and Technology, University of Electronic Science and Technology of China, Chengdu 610051, China (e-mail: shi_shaolong@163.com).

Yifan Chen is with the School of Life Science and Technology, University of Electronic Science and Technology of China, Chengdu 610051, China, and also with the School of Engineering, University of Waikato, Hamilton 3216, New Zealand (e-mail: yifan.chen@uestc.edu.cn).

Xin Yao is with the Department of Computer Science and Engineering, Southern University of Science and Technology, Shenzhen 518055, China, and also with the School of Computer Science, University of Birmingham, Birmingham B15 2TT, U.K. (e-mail: yaox@sustech.edu.cn).

Color versions of one or more of the figures in this article are available online at http://ieeexplore.ieee.org.

Digital Object Identifier 10.1109/TCYB.2020.3024868

I. INTRODUCTION

A. Background

CANCER refers to the abnormal and uncontrolled cell growth due to an accumulation of specific genetic and epigenetic defects [1]. It has been a leading cause of death globally for many years [2]. As many cancers are diagnosed only after they have metastasized throughout the body, effective and accurate methods of early stage cancer detection and clinical diagnosis are urgently needed [3]. Early detection of tissue malignancy can increase greatly the chances for successful treatment and it is particularly relevant for cancers of breast, cervix, mouth, larynx, colon and rectum, and skin. For example, the five-year survival rate is 90% if colorectal cancer is diagnosed while still localized (i.e., confined to the wall of the bowel) but reduces to only 68% for regional disease (i.e., disease with lymph node involvement) and only 10% if distant metastases are present [4]. The conventional imaging technology of cancer detection, such as ultrasound, computed tomography, positron emission tomography, and magnetic resonance imaging (MRI), has limitations in terms of tumor grading and molecular characterization as they are not designed to image a small number of cancer cells [5]–[7]. Therefore, early detection and localization of solid tumors (e.g., sarcomas, carcinomas, and lymphomas) that may exist in most organs and tissues of the body cannot be achieved by the conventional imaging modalities, and this is our starting point.

Nanoparticles are organic or inorganic, metallic, magnetic, or even polymeric particles with a diameter of less than 100 nm [8]. Nanoparticles exhibit several unique properties that can be applied to develop chemical and biological sensors possessing desirable features like enhanced sensitivity and lower detection limits [9]. They can cross barriers, such as blood-brain barrier or gastrointestinal barrier, which is a major advantage for the detection and visualization of tumor cells at very early stages, ideally at the level of a single cell or multiple cells [8], [10]. For example, Liu *et al.* [11] developed a nanosensor that detected carcinoembryonic antigen as a model protein, which showed potential applications for early diagnosis of diseases. Several studies have also been carried out on early detection of tumor cells *via* the attachment of proteins expressed in a very high quantity of cancer cells [12], [13]. These novel nanoscale platforms possess excellent physiochemical properties and offer prolonged circulation times and improved absorption rates. However, these nanoparticles are circulated systemically and, thus, exhibit poor targeting efficiency for precise localization of the lesion [14], [15].
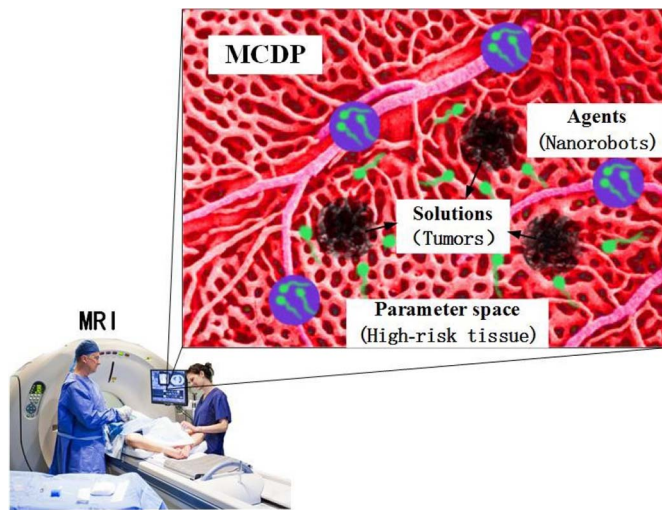
Fig. 1. Pictorial illustration of the MCDP model.

Enhancing the diagnostic efficacy of nanoparticles necessitates the use of guidance technologies, which demand effective controlling and tracking of nanoparticles. This, in turn, calls for the integration of sensing and actuation mechanisms at the nanoscale.

Recent decades have witnessed enormous progress in the manipulation of nanorobots in the *in vivo* environment for externally controllable early cancer detection [16]. Due to their small size, however, individual nanorobots are limited in their operational ranges and sensing capabilities. Nanorobots must work together to cover large areas and perform complex functionalities, which can be achieved through swarm intelligence [16]–[18]. Furthermore, so far, very few groups have succeeded in developing a fully autonomous (i.e., without the need for an external power source for propulsion) nanorobot capable of effective thrust in practical applications. To overcome these constraints, bioinspired, biocompatible, and biodegradable nanorobots, such as flagellated magnetotactic bacteria (MTB) with nanometer-sized magnetosomes, have been proposed [19]–[21]. A swarm of MTB can be guided and tracked by an external monitoring device, such as a customized MRI system to deliver drug-containing nanoliposomes to the target areas, which can significantly improve the therapeutic index of various nanocarriers in tumor regions as demonstrated in [20]. However, to the best of our knowledge, there has not been any experimental work in the existing literature on applying nanorobots for effective early cancer detection. This may be due to the fact that the destination is known as *a priori* in targeted drug delivery, which provides a clear direction for generating the guiding field. On the other hand, the knowledge of the location (or even presence) of tissue malignancy is not available in early cancer detection, which significantly increases the complexity of system design.

Recently, we have proposed a novel framework of computing-inspired biodetection, also called "Touchable Computing" (TouchComp) [22], which attempts to shed some theoretical insight on nanorobots-assisted, "smart" tumor sensing. TouchComp extends the idea of swarm intelligence to externally controllable biosensing, and improves the detection efficiency compared to the random search strategy relying on systemic circulation without making use of any intelligence about the biological, chemical, or physical phenomenon induced by cancer cells [19], [22], [23]. The central idea of TouchComp is summarized in Fig. 1. Consider the case of a multifocal cancer detection procedure (MCDP). The tumor foci are the regions of interests (ROIs) in a high-risk tissue region. The tumors trigger certain *in vivo* phenomena that can be detected by observing the properties of a swarm of nanorobots deployed due to the interaction between the nanorobots and the environment. TouchComp aims to coordinate the movement of all nanorobots through specific schemes of swarm intelligence in order to search for the ROIs effectively.

B. Main Contributions of the Current Work

Different from our previous work, which focuses on the detection of a single cancer [22], we look into the multimodal biodetection scenario (i.e., MCDP) in our present work. Multifocal tumors are not multiple tumors; they originate from a unique cellular clone and grow multifocally in a single organ (liver, kidney, thyroid, etc.) [24]. As shown in Fig. 1, the solutions are the tumor foci to be detected; the parameter space representing all possible solutions is the tissue region at a high risk of malignancy; the externally maneuverable agents are nanorobots, such as MTB. The agents (i.e., nanorobots) locate all the optimal solutions (i.e., tumors) by moving through the parameter space (i.e., high-risk tissue) under the guidance of an exterior steering field (i.e., MRI).

Different from the classical mathematical computing that uses ideal noninteracting agents, the landscape for the MCDP that corresponds to a biological, chemical, or physical cost function induced by tumors may be altered by agents due to the *natural computing* feature of MCDP, where agents interact with the solution space (i.e., nanorobots undergo reactions in the *in vivo* environment). An external observer can then infer the landscape for cancer detection by monitoring the movement of agents, which is called "seeing-is-sensing" in [21]. Provided with this analogy, a wide variety of computational techniques can thus be applied to the design of optimal MCDP.

The genetic algorithm (GA) is a metaheuristic inspired by the process of natural selection, which generates high-quality solutions to optimization and search problems by relying on bioinspired operators, such as mutation, crossover, and selection [25]. Niching methods allow the GA to maintain a population of diverse individuals, which can be used in domains that require the maintenance of multiple solutions [26]. In this article, the niche GA (NGA) is considered and introduced into the MCDP with the assumption that the landscape of the tissue region under surveillance is nonlinear and multimodal. Furthermore, we modify the crossover strategy of the standard NGA by dividing the initial population into two groups and implementing crossover between groups to improve the performance of tumor detection.

This article is organized as follows. In Section II, we establish the foundation of computing-inspired MCDP by extending the modeling of single cancer detection proposed in [22] to

multifocal cancer detection. In particular, we employ externally controllable nanorobots moving in the blood vessels to indicate the blood flow velocity that cannot be imaged by conventional imaging techniques because of their low resolutions [5], [6], [19], [27]. A multiple hump function with three global minima and its two variants are employed to represent the distribution of blood flow velocity in the presence of cancerous tissues as described in [28]–[30]. In Section III, we propose the NGA-inspired MCDP following the problem setting presented in Section II and modify the standard NGA from the algorithmic perspective, which is different from the method used in [22] for single cancer detection. In Section IV, some numerical examples are provided to demonstrate the principles and effectiveness of the proposed framework. Finally, some conclusive remarks are drawn in Section V.

II. Computing-Inspired MCDP

The framework of computing-inspired biodetection builds upon the similarity between the evolutionary computational process and the nanorobots-assisted MCDP. An evolutionary system can be seen as a process that, given particular initial conditions, follows a trajectory over time through a complex evolutionary state space to develop problem solvers automatically [25]. The swarm of nanorobots can be seen as an evolutionary system with the aim to accomplish the biodetection in an efficient and robust manner. More specifically, an aggregation of nanorobots loaded with contrast medium molecules is injected into the high-risk tissue, which corresponds to the initialization step of the evolutionary system. The nanorobots swim in the *in vivo* environment following certain trajectories to search for the tumors and the process is monitored by an external macroscale device. To evaluate the chance of finding tumors by nanorobots at specific locations, the concept of "fitness function" in mathematics and computer science is introduced. As the existing experimental results show that the velocity of blood flow in which nanorobots exist usually increases with the distance from cancer as to be elaborated further in Section II-B, the "fitness" of a nanorobot is negatively correlated with the blood flow velocity it experiences. Subsequently, the nanorobots update their locations in the tissue region under surveillance according to their fitness values. When a tumor is detected by a nanorobot, the nanorobot will adhere to the tumor and appears to stop moving (i.e., its velocity observed by the external monitoring system reduces to zero). It is worth noting that the reduction of blood flow velocity alone does not necessarily mean that there is a tumor; only a complete stop of a nanorobot indicates the presence and location of a tumor. Subsequently, the nanorobots-assisted MCDP can be formulated as a stylized representation of the general problem of agents-aided solution searching in the parameter space [22].

A. Problem Formulation

Consider a general parameter space $\mathcal{P}$ with the following agent-dependent landscape [22]:

$$o(\vec{x}; A) = o_{ms}(\vec{x}; A) + o_{\text{fit}}(\vec{x}; A)$$
$$= o_{\text{in}}(\vec{x}) + o_{ex}(\vec{x}; A) + o_{\text{fit}}(\vec{x}; A), \vec{x} \in \mathcal{P} \quad (1)$$

where $o_{ms}(\vec{x}; A)$ is the externally measurable objective function at location $\vec{x}$ for agent A, $o_{\text{in}}(\vec{x})$ is the intrinsic objective function at $\vec{x}$ independent of the presence or absence of A, $o_{ex}(\vec{x}; A)$ is the extrinsic disturbance to the landscape caused by the interaction between A and the parameter space $\mathcal{P}$, and $o_{\text{fit}}(\vec{x}; A)$ is the correction factor accounting for the *activeness* of A, due to its degradation in $\mathcal{P}$. The computing-inspired model of MCDP can be expressed as follows: given a search space (i.e., high-risk tissue) $\mathcal{P}$, the agents move through the search space to locate the targets (i.e., tumors). It is assumed that the tumor locations remain unchanged regardless of any variation caused by agents to the landscape. Nanorobots can bind to tumor cell receptors when they detect the tumors and stop moving, indicating the termination of the MCDP. Furthermore, we use the velocity of blood flow as the objective function to define the fitness of nanorobots. Subsequently, the MCDP can be seen as a procedure to search for the minimum values of the objective function

$$\min_{\vec{x} \in \mathcal{P}} o(\vec{x}; A). \quad (2)$$

In the MCDP, an optimization or niching method aims to locate all possible $\vec{x}^* \in \mathcal{P}$ (i.e., identifying all the tumors), which result in the smallest possible objective values

$$o(\vec{x}^*; A) \le o(\vec{x}; A) \quad \forall \vec{x} \in \mathcal{P}. \quad (3)$$

The mapped o values in the immediate vicinity of an $\vec{x}^*$ should be all equal or higher than $o(\vec{x}^*; A)$. The corresponding solution set is denoted as $\mathcal{S}$.

More specifically, N nanorobotic agents $A_1, A_2, \ldots, A_N$ are injected into the capillary around the high-risk tissue as shown in Fig. 1. The agents are employed to search for the solution set $\mathcal{S}$, with their initial locations $\vec{x}_1(t_0), \vec{x}_2(t_0), \ldots, \vec{x}_N(t_0)$ at the initial time t_0. The initial speed of A_n ($n = 1, 2, \ldots, N$) is $v_n(\vec{x}_n(t_0))$), which is assumed to be equal to the blood flow velocity at $\vec{x}_n(t_0)$, as blood has a low Reynolds coefficient and the inertia force of agents can be ignored compared to the viscosity force [31]. The location of agent A_n can be updated according to (4) as the capillary network of the healthy tissue is grid like [22]

$$\vec{x}_n(t_{k+1}) = \vec{x}_n(t_k) + d_n(t_k, t_{k+1})\vec{u}_{\angle \phi_F(\vec{x}_n(t_k)) + \phi_P(\vec{x}_n(t_k))}$$
$$= \vec{x}_n(t_k) + \sum_{l=1}^{L_n(t_k, t_{k+1})} v_n(\vec{x}_n(t_k))\delta t_{n,l}(t_k, t_{k+1})$$
$$\times \vec{u}_{\angle \phi_{n,l}(t_k, t_{k+1})}. \quad (4)$$

As illustrated in Fig. 2, when A_n does not meet the target, it will move continuously from $\vec{x}_n(t_k)$ at time t_k to $\vec{x}_n(t_{k+1})$ at time t_{k+1} in one iteration. The path of the nanorobot is composed of some linear segments. The term $d_n(t_k, t_{k+1})$ in (4) is the displacement length of A_n from $\vec{x}_n(t_k)$ to $\vec{x}_n(t_{k+1})$, $L_n(t_k, t_{k+1})$ is the number of piecewise-linear sections along the trajectory of A_n from $\vec{x}_n(t_k)$ to $\vec{x}_n(t_{k+1})$ in the search space; the traveling time of the lth linear section is $\delta t_{n,l}(t_k, t_{k+1})$ that satisfies $\sum_{l=1}^{L_n(t_k, t_{k+1})} \delta t_{n,l}(t_k, t_{k+1}) = t_{k+1} - t_k = \triangle t$, where $\triangle t$ is the iteration period of the external steering field; and $\vec{u}_{\angle \phi}$ is a unit vector with angle ϕ. The objective functions obtained by all agents are computed according to (1). When A_n meets
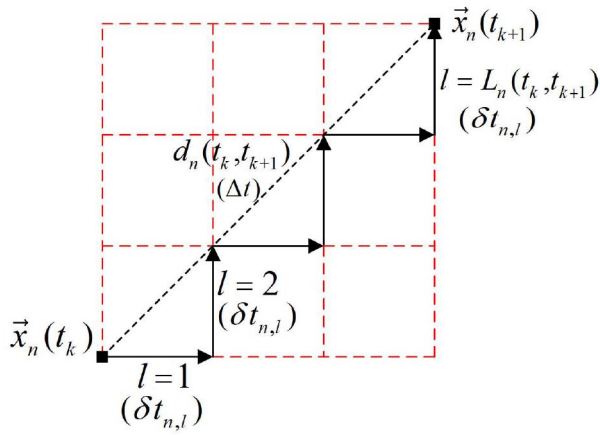
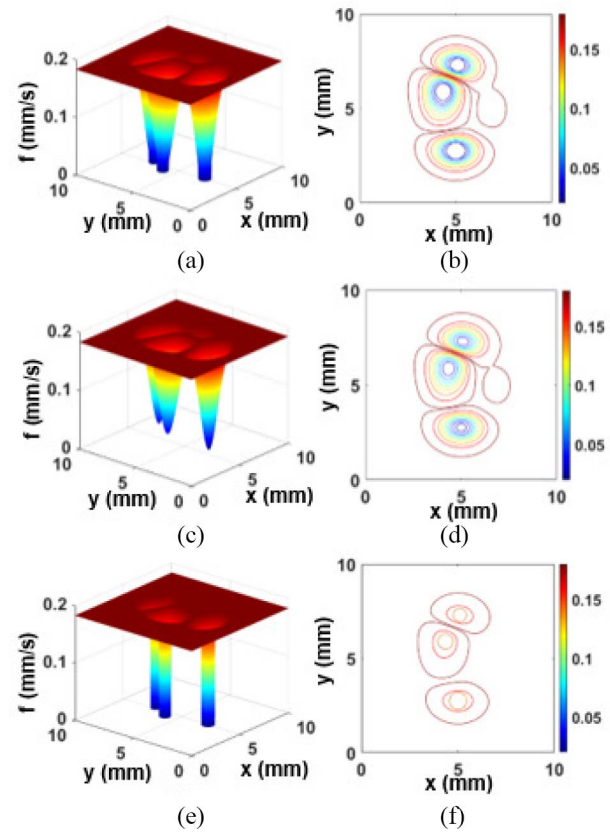Fig. 2. Update of the location of agent A_n in one iteration.

Fig. 3. Three-dimensional plot of the three artificial landscapes are shown as (a), (c), and (e); and blood velocity contours of the parameter space are shown as (b), (d), and (f).

the solution set $\mathcal{S}$ (i.e., a tumor is detected by a nanorobot), the stopping criteria are met. Otherwise, A_n will continue to move according to (4). A new agent will be randomly deployed within the injected area to ensure a constant number of agents in the medium, if an old agent fully degenerates.

B. Landscape of Parameter Space

The blood flow rate in a vascular network is proportional to the pressure difference between the arterial and venous sides and inversely proportional to the viscous and geometric resistances. Microvascular pressures in the arterial side are nearly equal in tumor and nontumorous vessels. Pressures in venular vessels are significantly lower in a tumor than those in a nontumorous tissue [32]. The presence of tumors can thus affect the distribution of blood flow velocity in the capillaries of the high-risk tissue. The blood flow velocity was shown to decrease significantly when blood enters the tumors (dropping from 183.4 ± 35.0 μm/s to 114.1 ± 26.1 μm/s) and then soon return to the prior level upon flowing out of the tumors [33]. Furthermore, the blood flow near malignant tumors has been studied using radioactive ^{90}Y microspheres while treating patients. The qualitative investigation demonstrates a normal tissue flow/tumor flow ratio in the range of 3/1 to 30/1. In addition, the peripheral tumor areas show a higher flow rate than more central portions [29], [34].

Based on the aforementioned phenomena, we consider a representative artificial landscape to evaluate the performance of MCDP, which synthesizes the scenario of the blood flow variation around the tumor foci and can be regarded as the biological cost function to be optimized. In other words, the landscape shown in Fig. 3 can be used to represent $f(\vec{x}) = o(\vec{x}; A)(\text{mm/s})$, where $\vec{x} = (x, y)$ is in mm and the parameter range is $0 \leq x, y \leq 10$ mm.

As shown in Fig. 3(a) and (b), landscape I with three different humps represents the situation that there are three tumor foci. The blood flow velocity decreases with the distance from the centers of the three tumors, (5.1, 7.3), (4.4, 5.9), and (5, 2.8), respectively. Furthermore, landscape II is used to represent the scenario that the objective function values are nonzero around the tumors because of some uncertainties in the sensing process, and landscape III is used to represent the

scenario that the blood velocity is high and decreases rapidly around the tumors. The objective functions are expressed as follows [35].

Landscape I:

$$f(\vec{x}) = \begin{cases} 0, & \sqrt{(x-5.1)^2 + (y-7.3)^2} \leq 0.1\sqrt{3} \\ 0, & \sqrt{(x-4.4)^2 + (y-5.9)^2} \leq 0.1\sqrt{4} \\ 0, & \sqrt{(x-5)^2 + (y-2.8)^2} \leq 0.1\sqrt{5} \\ -|f_1(\vec{x}) + f_2(\vec{x}) + f_3(\vec{x})| + 0.18, & \text{Otherwise.} \end{cases}$$

(5)

Landscape II:

$$f(\vec{x}) = -0.8|f_1(\vec{x}) + f_2(\vec{x}) + f_3(\vec{x})| + 0.18. \quad (6)$$

Landscape III:

$$f(\vec{x}) = \begin{cases} 0, & \sqrt{(x-5.1)^2 + (y-7.3)^2} \leq 0.1\sqrt{3} \\ 0, & \sqrt{(x-4.4)^2 + (y-5.9)^2} \leq 0.1\sqrt{4} \\ 0, & \sqrt{(x-5)^2 + (y-2.8)^2} \leq 0.1\sqrt{5} \\ -0.2|f_1(\vec{x}) + f_2(\vec{x}) + f_3(\vec{x})| + 0.18, & \text{Otherwise} \end{cases}$$

(7)

where

$$f_1(\vec{x}) = 0.1(6-x)^2 \exp\left[-(x-5)^2 - (y-6)^2\right] \quad (8)$$

This article has been accepted for inclusion in a future issue of this journal. Content is final as presented, with the exception of pagination.

SHI *et al.*: NGA-INSPIRED NANOROBOTS-ASSISTED DETECTION OF MULTIFOCAL CANCER

5

$$f_2(\vec{x}) = -0.01\Big[x/5 - (x-5)^3 - (y-5)^5 - 1\Big]^2$$
$$\times \exp\Big[-(x-5)^2 - (y-5)^2\Big] \tag{9}$$
$$f_3(\vec{x}) = 0.05 \exp\Big[-(x-4)^2 - (y-5)^2\Big]. \tag{10}$$

C. Capillary Network Model of Tumors

In tumor vasculature, the large surface areas of capillaries make them the ideal site to provide nutrients and oxygen for the growth of tumors [36]. For tumors, angiogenesis appears to be a critical determinant of growth, invasion, and metastatic potential [37]–[39]. The angiogenic activity is located within a few hundred micrometers from the tumor rim. Fueling further growth, the resulting neovasculature is progressively coopted together with the original blood vessels by the expanding tumor mass while also pushing the neovascularization zone further into normal tissue [40]. The hastily formed new tumor microcirculation is always different from the host vasculature due to the influence of tumor angiogenesis factors and the reduction of the available oxygen and nutrients [32], [41]–[43]. Hence, tumors are known to contain many tortuous vessels, shunts, vascular loops, widely variable intervascular distances, and large avascular areas, while normal capillaries are almost uniformly distributed to ensure adequate oxygen and nutrients transportation through the tissue [44]. The microvascular density is greater in the periphery of the highly vascularized tumor than that of the surrounding normal tissue [45]. These characteristics of tumor vasculature are well synthesized by the invasion percolation method, which is a classical statistical growth process governed by local substrate properties [46].

The simulation of vascular growth begins with a square lattice of discrete points that represents potential paths of vascular growth. Invasion percolation is implemented by first assigning uniformly distributed random values or strengths to each point on the underlying lattice. Starting at an arbitrary point the network occupies the lattice point adjacent to the current network that has the lowest strength. Growth is iterated until the desired lattice occupancy is reached. Blood vessels are assumed to connect all adjacent occupied lattice points. Blood is supplied at the starting point and withdrawn from the point nearest to the opposite corner. The network is then pruned to retain only those parts of the network with nonzero flow, leaving what is known as the "backbone" of the percolation cluster. Fig. 4 depicts the invasion percolation result after 260 growth steps, which also shows the backbone of the percolation clusters after pruning the vessels with zero blood flow.

It is a common strategy to restrict the vessels to run only parallel to the coordinate axes in modeling microvasculature [42], [45], [47], [48]. Subsequently, it is appropriate to model the tumor capillary network using the latticed model with a fixed microvascular density for normal tissues and a greater microvascular density for the periphery of tumors. In this way, we simulate the tumor-induced angiogenesis for the blood flow velocity profiles as shown in Fig. 5. The global capillary network is a square with an area of 10 mm × 10 mm. There are three different tumor foci *T*1, *T*2, and *T*3, which are
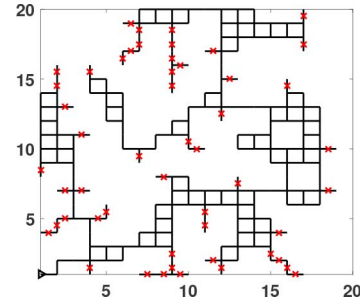

Fig. 4. Computer-generated percolation network after 260 growth steps of occupancy after pruning of vessels with zero blood flow.
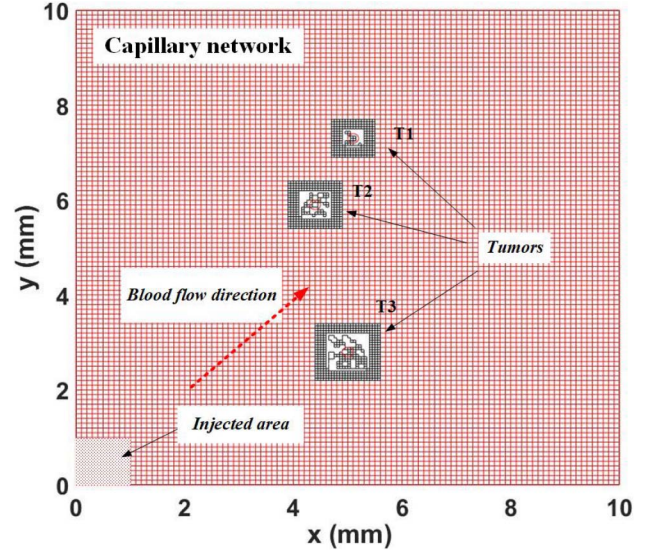

Fig. 5. Simulated vascular network for the blood flow velocity profiles. The vasculature is created by regular space-filling arrays with different microvascular densities representing normal and peritumoral tissues and invasion-percolation-based structure representing tumor tissues with a reduced microvascular density. The tumor foci centers are denoted by the red circles.

represented by three different square areas. The center coordinates of the tumors are (5.1, 7.3), (4.4, 5.9), and (5, 2.8) and the side lengths are 0.8, 1, and 1.2 mm, respectively. The centers of the tumor foci where the velocity of nanorobots becomes zero are three circular areas with a radius of 100 μm. We define the intercapillary distances to be 100 μm for the normal capillary network and 50 μm for capillaries in the periphery of the tumors. The periphery we define here corresponds to the blood velocity contour with the value of 60 μm/s. The level of occupancy on the lattice is chosen to be 60% before pruning [46]. For each vascular element in Fig. 5, the flow rate is assumed to follow Poiseuille's law. A number of capillary elements come together at each node, which satisfies mass conservation and therefore the sum of all flows at each node is zero. The general direction of blood flow is from the bottom left coordinate (0, 0) to the top right coordinate (10, 10), which is 45° to the *x* and *y* axes, respectively, as shown in Fig. 5.

III. NGA-INSPIRED MCDP

The GA first proposed and analyzed by Holland in 1975 is commonly used to solve optimization

---

Algorithm 1 Pseudocode of s-NGA

1: Choose an initial population $A_1, A_2, \ldots, A_N$ with their initial locations $\vec{x}_1^0, \vec{x}_2^0, \ldots, \vec{x}_N^0$
2: Evaluate fitness of agents $A_1, A_2, \ldots, A_N$.
3: **for** k less than the initialized iteration number K **do**
4:     Use normal genetic operators to get new positions $\vec{x}_1^{(k+1)}, \vec{x}_2^{(k+1)}, \ldots, \vec{x}_N^{(k+1)}$ of new agents
5:     Replace the old agents (positions $\vec{x}_1^k, \vec{x}_2^k, \ldots, \vec{x}_N^k$) with new agents (positions $\vec{x}_1^{(k+1)}, \vec{x}_2^{(k+1)}, \ldots, \vec{x}_N^{(k+1)}$)
6:     Use niching technology in agents:
7:     **while** $Distance(\vec{x}_i^{(k+1)}, \vec{x}_j^{(k+1)}) \leq L$ **do**
8:         Penalize the worse agent
9:     **end while**
10:     Evaluate fitness of agents (the initial population of next generation) at positions $\vec{x}_1^{(k+1)}, \vec{x}_2^{(k+1)}, \ldots, \vec{x}_N^{(k+1)}$
11: **end for**

Algorithm 2 Pseudocode of m-NGA

1: Choose two initial populations $A_1, A_2, \ldots, A_M$ and $A_{M+1}, A_{M+2}, \ldots, A_N$ with their initial locations $\vec{x}_1^0, \vec{x}_2^0, \ldots, \vec{x}_M^0$ and $\vec{x}_{M+1}^0, \vec{x}_{M+2}^0, \ldots, \vec{x}_N^0$
2: Evaluate fitness of agents $A_1, A_2, \ldots, A_N$.
3: **for** k less than the initialized iteration number K **do**
4:     Use normal genetic operators with crossover between two groups to get new positions $\vec{x}_1^{(k+1)}, \vec{x}_2^{(k+1)}, \ldots, \vec{x}_M^{(k+1)}$ and $\vec{x}_{M+1}^{(k+1)}, \vec{x}_{M+2}^{(k+1)}, \ldots, \vec{x}_N^{(k+1)}$ of new agents.
5:     Replace the old agents (positions $\vec{x}_1^k, \vec{x}_2^k, \ldots, \vec{x}_M^k$ and $\vec{x}_{M+1}^k, \vec{x}_{M+2}^k, \ldots, \vec{x}_N^k$) with new agents (positions $\vec{x}_1^{(k+1)}, \vec{x}_2^{(k+1)}, \ldots, \vec{x}_M^{(k+1)}$ and $\vec{x}_{M+1}^{(k+1)}, \vec{x}_{M+2}^{(k+1)}, \ldots, \vec{x}_N^{(k+1)}$).
6:     Use niching technology in agents:
7:     **while** $Distance(\vec{x}_i^{(k+1)}, \vec{x}_j^{(k+1)}) \leq L$ **do**
8:         Penalize the worse agent
9:     **end while**
10:     Evaluate fitness of agents (the initial population of next generation) at positions $\vec{x}_1^{(k+1)}, \vec{x}_2^{(k+1)}, \ldots, \vec{x}_N^{(k+1)}$
11: **end for**

---

problems [25], [49], [50]. As an effective method for solving complex problems, once the genetic representation and the fitness function are defined, a GA proceeds to initialize a population of solutions and then to improve it through repetitive application of the mutation, crossover, inversion, and selection operators [51].

However, traditional GAs will push an artificial population toward convergence through natural evolutionary processes maintain a variety of species with each occupying a separate ecological niche. In nature, a niche is viewed as an organism's task in the environment, and a species is a collection of organisms with similar features. The subdivision of the environment on the basis of an organism's role helps stable subpopulations to form around different niches in the environment [52]. The niching technique has recently been introduced into GAs to make it possible to find more than one local optimum of a multimodal landscape. Niching technology can make individuals evolve in a special environment by adjusting the fitness of individuals and the replacement strategy to generate the new generation. This method can maintain the diversity of the evolution population and acquire multiple solutions at the same time. Three general niching techniques: 1) preselection; 2) crowding; and 3) fitness sharing are popular. The standard NGA (s-NGA) is widely used in the multimodal and nonmonotonic function optimization. In s-NGA, a niche is commonly referred to as the location of each optimum in the search space, and the fitness represents the resource of that niche. The organisms in a niche can be defined as similar individuals in terms of similarity metrics. The pseudocode of s-NGA is given in Algorithm 1.

As for the selection operator, we use the method of roulette wheel selection, which is the first selection method developed by Holland [44]. The probability of selection for each individual i, P_i, is defined by

$$P_i = \frac{F_i}{\sum_{j=1}^{N} F_j} \tag{11}$$

where F_i is equal to the fitness of individual i. As for the crossover operator, we use a traditional two-parent crossover operator and characterize the result of this process using real-value coding. The N individuals are paired at random, yielding $N/2$ couples. For each couple, crossover may or may not occur. Crossover does not occur with the probability of $1 - p_c$. Subsequently, both individuals proceed to the mutation stage. Otherwise, the couple generates two children *via* crossover, and only the children continue to the mutation stage. The crossover and mutation processes are as follows:

$$\begin{cases} \vec{x}_n^{(k+1)} = \alpha \vec{x}_n^k + (1-\alpha)\vec{x}_{n+1}^k \\ \vec{x}_{n+1}^{(k+1)} = \alpha \vec{x}_{n+1}^k + (1-\alpha)\vec{x}_n^k \end{cases} \tag{12}$$

$$\vec{x}_n^{(k+1)} = \vec{x}_n^k + \sigma \tag{13}$$

where α follows a uniform distribution between 0 and 1 [i.e., $\alpha \sim U(0, 1)$], and σ follows a Gaussian distribution with mean 0 and variance 1 [i.e., $\sigma \sim N(0, 1)$]. Then, we use a niching method with the modified crowding scheme to preserve population diversity. In crowding, each individual is compared to its neighbor within a constant distance, and the worse one is punished with less opportunity to produce an offspring. Inspired by the physiological viewpoint that offspring resulting from inbreeding tends to be unhealthy, we further propose a modified NGA (m-NGA). In the algorithm, the initial population is separated into two groups with the same number of individuals randomly; each individual in one group can only perform crossover with an arbitrary individual in another group; the rest of the processes is similar to the s-NGA. The m-NGA is represented in the pseudocode of Algorithm 2.

In the following, we will formulate the MCDP based on a similar evolutionary mechanism with the aforementioned NGAs but taking into account realistic *in vivo* propagation, controlling, and tracking scenarios.

Nanorobots loaded with contrast medium molecules are injected into the tissue region. The injection area is a 1 mm × 1 mm square as shown in Fig. 5. Each nanorobot adjusts its own location based on the comparison with its offspring location under the influence of the blood flow and the external magnetic field. Fig. 6 gives the movement direction of agent A_n in MCDP. The location of A_n at step k is denoted by the vector $\vec{x}_n^k$; the ideal child location of A_n following the NGA
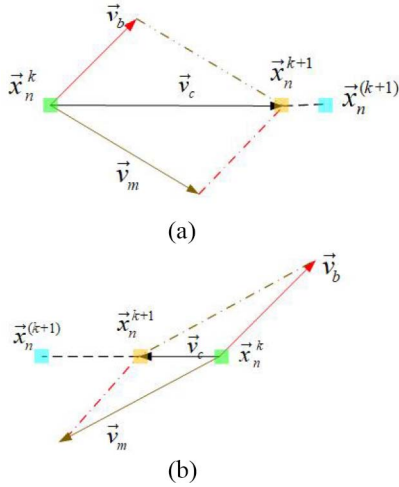
Fig. 6. Update of the location of a nanorobot: (a) angle between the directions of the blood flow and the magnetic field is acute; and (b) angle between the directions of the blood flow and the magnetic field is obtuse.

Algorithm 3 MCDP Algorithm

1: Choose an initial population $A_1, A_2, \ldots, A_N$ with their initial locations $\vec{x}_1^0, \vec{x}_2^0, \ldots, \vec{x}_N^0$
2: Evaluate fitness of agents $A_1, A_2, \ldots, A_N$.
3: **for** k less than the initialized iteration number K **do**
4:     Use normal genetic operators to get new positions $\vec{x}_1^{(k+1)}, \vec{x}_2^{(k+1)}, \ldots, \vec{x}_N^{(k+1)}$ of new agents
5:     **while** the agents stopping criterion not met **do**
6:         Move agents toward the offspring locations $\vec{x}_1^{(k+1)}$, $\vec{x}_2^{(k+1)}, \ldots, \vec{x}_N^{(k+1)}$ with the same steps respectively and get the new positions of agents $\vec{x}_1^{k+1}, \vec{x}_2^{k+1}, \ldots, \vec{x}_N^{k+1}$
7:     **end while**
8:     Use niche technology in agents:
9:     **while** $Distance(\vec{x}_i^{k+1}, \vec{x}_j^{k+1}) \leq L$ **do**
10:         Penalize the worse agent
11:     **end while**
12:     Evaluate fitness of agents (the initial population of next generation) at positions $\vec{x}_1^{k+1}, \vec{x}_2^{k+1}, \ldots, \vec{x}_N^{k+1}$.
13: **end for**

---

is denoted by the vector $\vec{x}_n^{(k+1)}$ and the actual location of A_n following the MCDP is denoted by the vector $\vec{x}_n^{k+1}$. The blood velocity, the nanorobot's velocity subject to the magnetic field without the influence of blood flow, and their resultant velocity are denoted by $\vec{v}_b$, $\vec{v}_m$, and $\vec{v}_c$, respectively. Subsequently, agent A_n will move by one step in the direction of $\vec{v}_c$ and the new position of A_n denoted by $\vec{x}_n^{k+1}$ will be obtained. $\vec{x}_n^{k+1}$ then plays the role of the parent in the next generation. Following this process, each nanorobot updates its location step by step. Note that the capillary network of healthy tissue and the tumor capillary network used in the simulation procedure are discontinuous 2-D grids; therefore, all agents' locations are mapped to the locations associated with the nearest blood vessel.

Subsequently, agent A_n evolves according to the following equations:

$$\vec{u}_{\angle\phi}(\vec{x}_n^k) = \frac{\vec{x}_n^{(k+1)} - \vec{x}_n^k}{\left|\vec{x}_n^{(k+1)} - \vec{x}_n^k\right|} \tag{14}$$

$$\vec{x}_n^{k+1} = \vec{x}_n^k + \sum_{l=1}^{L_n} v_n \delta t_{n,l} \vec{u}_{\angle\phi_{n,l}}. \tag{15}$$

The index $n = 1, 2, \ldots, N$; $\phi(\vec{x}_n)$ denotes the angle generated by the co-force of the external magnetic field and the blood flow on agent A_n at $\vec{x}_n^k$, $\phi_{n,l}$ is the direction of the lth linear section, $\vec{u}_{\angle\phi}$ is a unit vector with angle ϕ, L_n is the number of piecewise-linear sections along the trajectory of the nth agent in one iteration and $\delta t_{n,l}$ is the traveling time of the lth linear section satisfying $\sum_{l=1}^{L_n} \delta t_{n,l} = \Delta t$ with Δt being the constant interval of the controlling cycle. Equation (14) is used to calculate the new movement direction of the agent A_n by taking into the agent's current position and its offspring position obtained by the NGA operators. Equation (15) is used to evaluate the updated position of the agent A_n given the steering field and the underlying vascular network.

From the above description, we can see that the ideal location of each new agent provides a direction for the movement of its parent nanorobot. Every parent nanorobot swims in the

direction of its offspring agent under the steering of the external magnetic field and the blood flow field. The key difference between the NGA-inspired MCDP proposed here and the NGA presented previously is the offspring used. For NGA, the offsprings can be at any random locations in the continuous searching space, while the offsprings produced in the MCDP are all in the locations of blood vessels as the nanorobots can only swim in the capillary network. The s-NGA-inspired MCDP is described in Algorithm 3.

The initial deployment region of all the agents (i.e., the injected area shown in Fig. 5) is confined within a small area due to the practical constraint of the NGA-inspired MCDP, which is different from the normal NGA where all the agents are distributed in the entire searching space in the initial stage. All the nanorobots swim in the high-risk tissue under the external magnetic field to detect tumor areas using the MCDP given above. In case any nanorobot travels outside the search space, a new nanorobot will be deployed in the initial area to keep the number of nanorobots unchanged. The escaped nanorobot will degrade in the human body without causing any harmful effect [22].

Inspired by m-NGA, we introduce the new crossover scheme into MCDP. In this scenario, the nanorobots employed are divided into two groups randomly chosen in the initial phase with the other processes being similar to the aforementioned MCDP algorithm.

IV. PERFORMANCE ANALYSIS

We use several numerical examples to elaborate on the NGA-inspired MCDP. The blood flow velocity profile presented in Section II-B and the vascular network model presented in Section II-C are applied to synthesize tumor angiogenesis. In the simulation, 12 nanorobots are employed to execute the MCDP. The small number of nanorobots is chosen to minimize any side effects resulting from an excessive
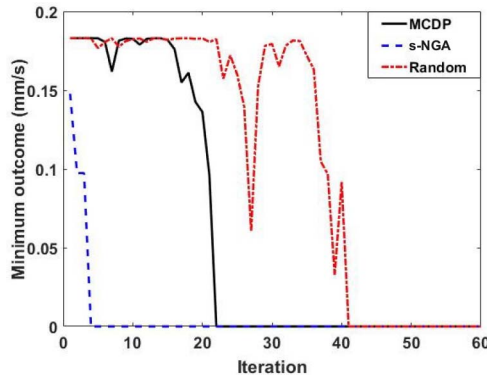
This article has been accepted for inclusion in a future issue of this journal. Content is final as presented, with the exception of pagination.

8   IEEE TRANSACTIONS ON CYBERNETICS

Fig. 7.   Minimum outcomes obtained over iterations.

Fig. 8.   Final positions of agents in the searching space.

amount of nanorobots on the human body. The initial injection area is $0 \leq x, y \leq 1$ mm as shown in Fig. 5. The initial speed of nanorobots is assumed to be 210 μm/s, which can be realized according to [19]. The period of iteration is set to be 4 s and the number of iterations is 60. The probabilities of crossover and mutation are 0.9 and 0.1, respectively. The crowding distance is set to be 0.15 mm.

Fig. 7 shows a typical curve of minimum outcomes obtained from the agents over multiple iterations for landscape I (the results of landscapes II and III are similar with that of landscape I) by using the s-NGA-inspired MCDP. It can be seen that an agent with the best performance can detect a tumor successfully at the 22nd iteration. To compare with the cancer detection method relying on systemic circulation without applying any metaheuristics under the same physical scenario, we also present the result obtained from the random searching strategy, which means the nanorobots swim in the capillary network without any external influence except the blood flow. In this case, we can see that the best agent can detect a tumor after 41 iterations, which is slower compared to the s-NGA-inspired MCDP. Furthermore, for comparison from the algorithmic perspective, we show the result for the s-NGA without any physical constraints. In this case, a target can be detected after four iterations.

Fig. 8 shows the final locations of agents after 60 iterations by using the three different algorithms. We can see that the agents in the s-NGA and MCDP algorithms have a good performance of clustering with nearly all the agents swarming around the different target areas. On the contrary, the agents in the random searching strategy are scattered in the searching space without any swarming behavior.

To provide statistical analysis of the robustness and precision of the s-NGA-inspired MCDP, we have carried out 1000 independent simulation runs. Fig. 9I-(a), II-(a), and III-(a) shows the histograms of the quantity of agents located at the targets for landscapes I, II, and III using the MCDP strategy with the means of 3.1, 2.7, and 2.5, and the variances of 4.2, 3.1, and 3.2, respectively. Fig. 9I-(b), II-(b), and III-(b) shows the histograms of the quantity of agents located at the targets for the three landscapes using the random searching strategy with the means of 1.7, 1.4, and 1.6, and the variances of 1.3, 1.5, and 1.7, respectively. Fig. 9I-(c), II-(c) and III-(c) shows the histograms of the quantity of agents
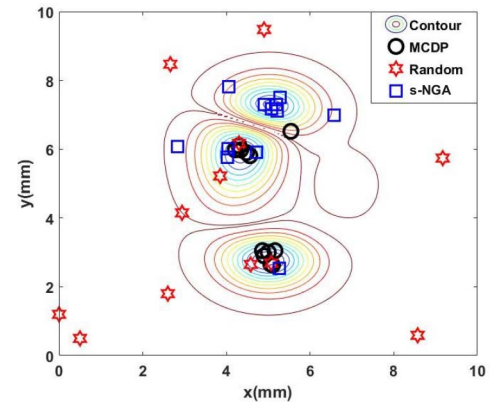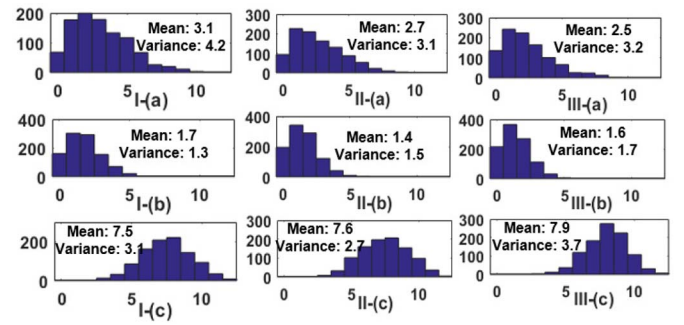

Fig. 9.   Histograms of the quantity of agents located at the tumor areas using the MCDP strategy are shown in I-(a), II-(a), and III-(a). Histograms of the quantity of agents located at the tumor areas using the random searching strategy are shown in I-(b), II-(b), and III-(b). Histograms of the quantity of agents located at the target areas using s-NGA are shown in I-(c), II-(c), and III-(c).

located at the targets for the three landscapes using the s-NGA with the means of 7.5, 7.6, and 7.9, and the variances of 3.1, 2.7, and 3.7, respectively. It is evident that the proposed MCDP significantly outperforms random searching in terms of the number of agents that can detect the cancer foci successfully. The performance of the MCDP strategy is not as good as the s-NGA, which is due to the fact that the MCDP is subject to various physical constraints. Furthermore, the performances of the MCDP for the three landscapes are similar, which demonstrates the robustness of the MCDP.

Fig. 10 shows the curves of minimum outcomes obtained from the agents over multiple iterations by using m-NGA, random searching, and MCDP algorithms. Comparing Fig. 10 with Fig. 7, it can be seen that the MCDP inspired by m-NGA performs worse than the one derived from the s-NGA in terms of the time spent in detecting a single tumor because of the decrease in exploitation for m-NGA. On the other hand, the other comparison results between the three methods are similar with the earlier observations.

Fig. 11 shows the final locations of agents after 60 iterations in the second case. It can be seen that the result in Fig. 11 is similar to that in Fig. 8.

Fig. 12 gives the histogram of the quantity of agents located at the tumor foci using the three algorithms in the second case. Though the observations made in Fig. 12 are somewhat similar with those from Fig. 9, it is interesting to note that the means in

This article has been accepted for inclusion in a future issue of this journal. Content is final as presented, with the exception of pagination.

SHI *et al.*: NGA-INSPIRED NANOROBOTS-ASSISTED DETECTION OF MULTIFOCAL CANCER
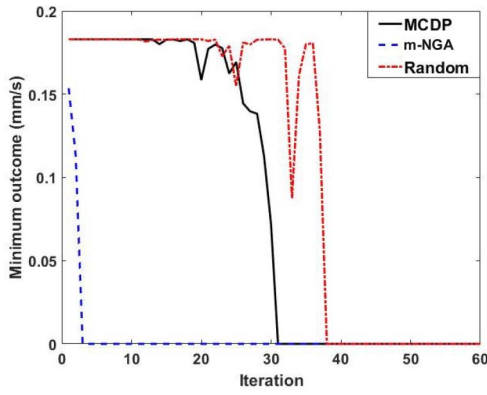
9

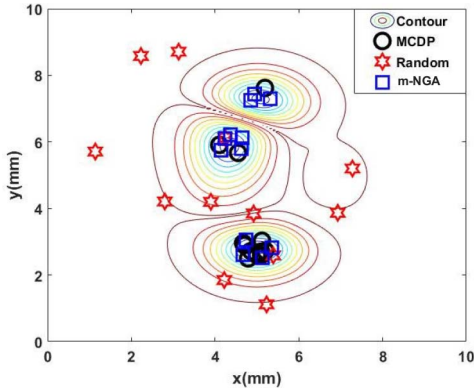Fig. 10. Minimum outcomes obtained over iterations.

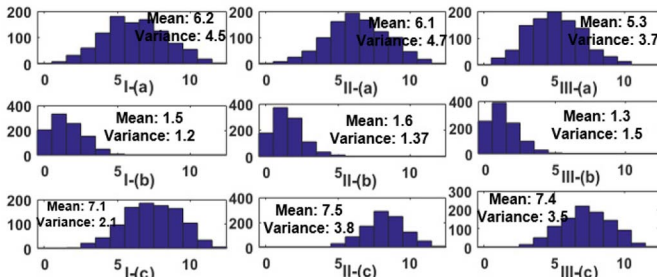Fig. 11. Final positions of agents in the searching space.

Fig. 12. Histograms of the quantity of agents located at the tumor areas using the MCDP strategy are shown in I-(a), II-(a), and III-(a). Histograms of the quantity of agents located at the tumor areas using the random searching strategy are shown in I-(b), II-(b), and III-(b). Histogram of the quantity of agents located at the target areas using m-NGA are shown in I-(c), II-(c), and III-(c).

the second case for MCDP are around 6 for three landscapes, which are larger than the values in Fig. 9I-(a), II-(a), and III-(a) due to the increase in exploration for m-NGA.

Fig. 13 presents the histograms of the quantity of nanorobots located at the three different tumors using the two different MCDP strategies. Fig. 13(a)–(c) shows the distribution of nanorobots located at the tumor foci $T1$, $T2$, and $T3$, respectively, by using the MCDP inspired by the s-NGA. Fig. 13(d)–(f) shows the distribution of nanorobots located at tumor foci $T1$, $T2$, and $T3$, respectively, by using the MCDP inspired by m-NGA. It is evident that for both the two strategies, the numbers of nanorobots in $T1$, $T2$, and $T3$ are increasing, which is in line with the sizes of the tumors
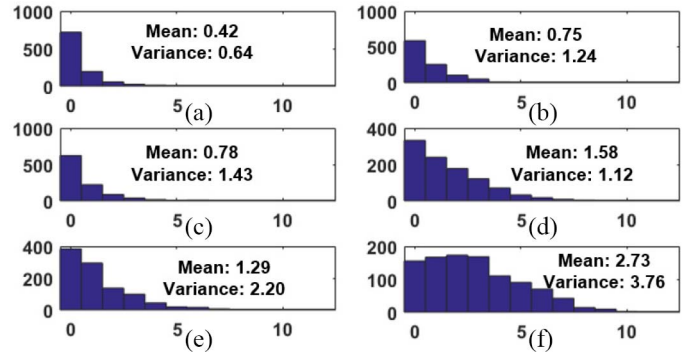

Fig. 13. Distribution of nanorobots at three different tumor areas $T1$ (a) and (d), $T2$ (b) and (e), and $T3$ (c) and (f) using two different MCDP strategies.
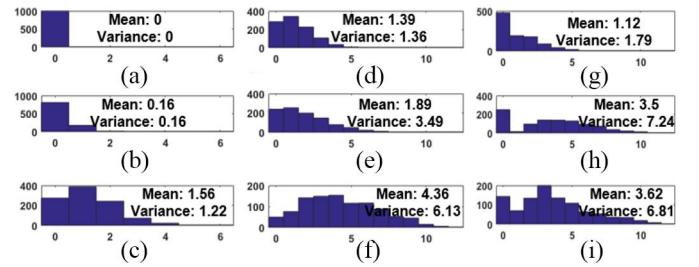

Fig. 14. Distribution of nanorobots at three different tumor areas $T1$ (a), (d), and (g); $T2$ (b), (e), and (h); and $T3$ (c), (f), and (i) using random searching, s-NGA, and m-NGA, respectively.

$T1 < T2 < T3$. For comparison, we also give the distribution of agents located at the tumor areas $T1$, $T2$, and $T3$, respectively, by using the random searching strategy, the s-NGA, and m-NGA, which is shown in Fig. 14. It is interesting to see that the numbers of nanorobots in $T1$, $T2$, and $T3$ are not adaptable to the tumors' area ratio for the random searching strategy. This is mainly caused by the relative orientations of the three tumors. For example, tumor $T1$ can be barely detected by any nanorobot under the random searching strategy because it is shadowed by tumor $T2$ without any line of sight to the injected area. The s-NGA and m-NGA both have good performances of target detection without any realistic physical constraint.

In summary, we can draw the conclusion that the MCDP performs better than random searching with realistic physical constraints from the biodetection perspective, while it performs worse than the s-NGA and m-NGA without realistic physical constraints from the algorithmic perspective. Furthermore, the MCDP inspired by m-NGA performs better than that inspired by the s-NGA.

V. CONCLUSION

We have presented the nanorobots-assisted detection of multifocal cancer from a multimodal optimization (MMO) perspective. Specifically, we have proposed the s-NGA-inspired MCDP by taking into account realistic *in vivo* conditions of nanorobots and characteristics of the vascular network around the tumor areas. Based on this work, we have also developed an m-NGA, which can be used to improve the performance of

MCDP. Numerical examples have demonstrated the effectiveness of the proposed methodology for the blood flow velocity profile induced by tumor angiogenesis.

Future work may include improving the performance of the algorithm to accomplish the detection of all the cancer areas with many more nanorobots. It is also important to examine further the impact of nanorobot nonidealities, such as finite lifespan, imprecise steering, and inaccurate tracking.

REFERENCES

[1] W. Schulz, *Molecular Biology of Human Cancers: An Advanced Student's Textbook*. Dordrecht, The Netherlands: Springer, 2005.

[2] I. Abubakar, T. Tillmann, and A. Banerjee, "Global, regional, and national age–sex specific all-cause and cause-specific mortality for 240 causes of death, 1990–2013: A systematic analysis for the global burden of disease study 2013," *Lancet*, vol. 385, no. 9963, pp. 117–171, 2015.

[3] B. Bohunicky and S. A. Mousa, "Biosensors: The new wave in cancer diagnosis," *Nanotechnol. Sci. Appl.*, vol. 4, no. 1, pp. 1–10, 2011.

[4] L. A. Ries *et al.*, *SEER cancer statistics review, 1975-2003*, Nat. Cancer Inst., Bethesda, MD, USA, 2006.

[5] J. V. Frangioni, "New technologies for human cancer imaging," *J Clin. Oncol.*, vol. 26, no. 24, pp. 4012–4021, 2008.

[6] F. Pakzad, A. Groves, and P. Ell, "The role of positron emission tomography in the management of pancreatic cancer," *Seminars Nucl. Med.*, vol. 36, no. 3, pp. 248–256, 2006.

[7] A. A. Bui and R. K. Taira, *Medical Imaging Informatics*. New York, NY, USA: Springer, 2009.

[8] M. Perfezou, A. Turner, and A. Merkoci, "Cancer detection using nanoparticle-based sensors," *Chem. Soc. Rev.*, vol. 41, no. 7, pp. 2606–2622, 2012.

[9] V. K. Khanna, "Nanoparticle-based sensors," *Defence Sci. J.*, vol. 58, no. 5, pp. 608–616, 2008.

[10] S. N. Tabatabaei, H. Girouard, A.-S. Carret, and S. Martel, "Remote control of the permeability of the blood–brain barrier by magnetic heating of nanoparticles: A proof of concept for brain drug delivery," *J. Controlled Release*, vol. 206, pp. 49–57, May 2015.

[11] M. Liu *et al.*, "Highly sensitive protein detection using enzyme-labeled gold nanoparticle probes," *Analyst*, vol. 135, no. 2, pp. 327–331, 2010.

[12] Z. Zhang *et al.*, "Three biomarkers identified from serum proteomic analysis for the detection of early stage ovarian cancer," *Cancer Res.*, vol. 64, no. 16, pp. 5882–5890, 2004.

[13] G. H. Lyman *et al.*, "American society of clinical oncology guideline recommendations for sentinel lymph node biopsy in early stage breast cancer," *J. Clin. Oncol.*, vol. 23, no. 30, pp. 7703–7720, 2005.

[14] J. D. Kingsley, H. Dou, J. Morehead, B. E. Rabinow, H. E. Gendelman, and C. J. Destache, "Nanotechnology: A focus on nanoparticles as a drug delivery system," *J. Neuroimmune Pharmacol.*, vol. 1, no. 3, pp. 340–350, 2006.

[15] G. Bao, S. Mitragotri, and S. Tong, "Multifunctional nanoparticles for drug delivery and molecular imaging," *Annu. Rev. Biomed. Eng.*, vol. 15, no. 1, pp. 253–282, 2013.

[16] Y. Okaie, T. Nakano, T. Hara, K. Hosoda, Y. Hiraoka, and S. Nishio, "Modeling and performance evaluation of mobile bionanosensor networks for target tracking," in *Proc. IEEE Int. Conf. Commun. (ICC)*, Sydney, NSW, Australia, 2014, pp. 3969–3974.

[17] S. Garnier, J. Gautrais, and G. Theraulaz, "The biological principles of swarm intelligence," *Swarm Intell.*, vol. 1, no. 1, pp. 3–31, 2007.

[18] I. F. Akyildiz, F. Brunetti, and C. Blazquez, "Nanonetworks: A new communication paradigm," *Comput. Netw.*, vol. 52, no. 12, pp. 2260–2279, 2008.

[19] S. Martel *et al.*, "MRI-based medical nanorobotic platform for the control of magnetic nanoparticles and flagellated bacteria for target interventions in human capillaries," *Int. J. Robot. Res.*, vol. 28, no. 9, pp. 1169–1182, 2009.

[20] O. Felfoul *et al.*, "Magneto-aerotactic bacteria deliver drug-containing nanoliposomes to tumour hypoxic regions," *Nat. Nanotechnol.*, vol. 11, no. 11, pp. 941–947, 2016.

[21] Y. Chen, T. Nakano, P. Kosmas, C. Yuen, A. V. Vasilakos, and M. Asvial, "Green touchable nanorobotic sensor networks," *IEEE Commun. Mag.*, vol. 54, no. 11, pp. 136–142, Nov. 2016.

[22] Y. Chen, S. Shi, X. Yao, and T. Nakano, "Touchable computing: Computing-inspired bio-detection," *IEEE Trans. Nanobiosci.*, vol. 16, no. 8, pp. 810–821, Dec. 2017.

[23] P. Vartholomeos, M. Fruchard, A. Ferreira, and C. Mavroidis, "Mri-guided nanorobotic systems for therapeutic and diagnostic applications," *Annu. Rev. Biomed. Eng.*, vol. 13, pp. 157–184, Aug. 2011.

[24] W. A. Berg and P. L. Gilbreath, "Multicentric and multifocal cancer: Whole-breast us in preoperative evaluation," *Radiology*, vol. 214, no. 1, pp. 59–66, 2000.

[25] K. A. De Jong, *Evolutionary Computation: A Unified Approach*. Cambridge, MA, USA: MIT Press, 2006.

[26] S. W. Mahfoud, "Niching methods for genetic algorithms," *Urbana*, vol. 51, no. 95001, pp. 62–94, 1995.

[27] S. Bipat *et al.*, "Colorectal liver metastases: CT, MR imaging, and pet for diagnosis–meta-analysis," *Radiology*, vol. 237, no. 1, pp. 123–131, 2005.

[28] G. Komar *et al.*, "Decreased blood flow with increased metabolic activity: A novel sign of pancreatic tumor aggressiveness," *Clin. Cancer Res.*, vol. 15, no. 17, pp. 5511–5517, 2009.

[29] D. B. Ellegala *et al.*, "Imaging tumor angiogenesis with contrast ultrasound and microbubbles targeted to $\alpha v \beta 3$," *Circulation*, vol. 108, no. 3, pp. 336–341, 2003.

[30] D. De Backer, J. Creteur, J.-C. Preiser, M.-J. Dubois, and J.-L. Vincent, "Microvascular blood flow is altered in patients with sepsis," *Amer. J. Respiratory Critical Care Med.*, vol. 166, no. 1, pp. 98–104, 2002.

[31] M. Sefidgar *et al.*, "Numerical modeling of drug delivery in a dynamic solid tumor microvasculature," *Microvasc. Res.*, vol. 99, pp. 43–56, May 2015.

[32] R. K. Jain, "Determinants of tumor blood flow: A review," *Cancer Res.*, vol. 48, no. 10, pp. 2641–2658, 1988.

[33] Y. Wang *et al.*, "Blood flow velocity is reduced in a tumor microdissemination in the visceral pleura in anesthetized open-chest rat lung," *Vivo*, vol. 23, no. 2, pp. 291–295, 2009.

[34] P. Vaupel, F. Kallinowski, and P. Okunieff, "Blood flow, oxygen and nutrient supply, and metabolic microenvironment of human tumors: A review," *Cancer Res.*, vol. 49, no. 23, pp. 6449–6465, 1989.

[35] A. P. Engelbrecht, *Fundamentals of Computational Swarm Intelligence*. Chichester, U.K.: Wiley, 2006.

[36] H. Rieger and M. Welter, "Integrative models of vascular remodeling during tumor growth," *Wiley Interdiscipl. Rev. Syst. Biol. Med.*, vol. 7, no. 3, pp. 113–129, 2015.

[37] B. R. Zetter, "Angiogenesis and tumor metastasis," *Annu. Rev. Med.*, vol. 49, no. 1, pp. 407–424, 1998.

[38] N. Weidner, J. Semple, W. Welch, and J. Folkman, "Tumor angiogenesis and metastasis–correlation in invasive breast carcinoma," *New England J. Med.*, vol. 324, no. 1, pp. 1–8, 1991.

[39] J. Folkman, "Tumor angiogenesis: Therapeutic implications," *New England J. Med.*, vol. 285, no. 21, pp. 1182–1186, 1971.

[40] M. Welter and H. Rieger, "Interstitial fluid flow and drug delivery in vascularized tumors: A computational model," *PLoS ONE*, vol. 8, no. 8, 2013, Art. no. e70395.

[41] P. Vaupel, H. Fortmeyer, S. Runkel, and F. Kallinowski, "Blood flow, oxygen consumption, and tissue oxygenation of human breast cancer xenografts in nude rats," *Cancer Res.*, vol. 47, no. 13, pp. 3496–3503, 1987.

[42] A. R. Anderson and M. Chaplain, "Continuous and discrete mathematical models of tumor-induced angiogenesis," *Bull. Math. Biol.*, vol. 60, no. 5, pp. 857–899, 1998.

[43] C. W. Song, "Effect of local hyperthermia on blood flow and microenvironment: A review," *Cancer Res.*, vol. 44, no. 10, pp. 4721s–4730s, 1984.

[44] Y. Gazit, D. A. Berk, M. Leunig, L. T. Baxter, and R. K. Jain, "Scale-invariant behavior and vascular network formation in normal and tumor tissue," *Phys. Rev. Lett.*, vol. 75, no. 12, pp. 2428–2431, 1995.

[45] D. S. Lee, H. Rieger, and K. Bartha, "Flow correlated percolation during vascular remodeling in growing tumors," *Phys. Rev. Lett.*, vol. 96, no. 5, 2006, Art. no. 058104.

[46] J. W. Baish, Y. Gazit, D. A. Berk, M. Nozue, L. T. Baxter, and R. K. Jain, "Role of tumor vascular architecture in nutrient and drug delivery: An invasion percolation-based network model," *Microvasc. Res.*, vol. 51, no. 3, pp. 327–346, 1996.

[47] T. L. Jackson, *Modeling Tumor Vasculature: Molecular, Cellular, and Tissue Level Aspects and Implications*. New York, NY, USA: Springer, 2011.

[48] J. W. Baish and R. K. Jain, "Fractals and cancer," *Cancer Res.*, vol. 60, no. 14, pp. 3683–3688, 2000.

[49] M. Mitchell, *An Introduction to Genetic Algorithms*. Cambridge, MA, USA: MIT Press, 1998.

[50] J. H. Holland, *Adaptation in Natural and Artificial Systems: An Introductory Analysis With Applications to Biology, Control, and Artificial Intelligence*. Cambridge, MA, USA: MIT Press, 1992.

[51] R. R. Bies, M. F. Muldoon, B. G. Pollock, S. Manuck, G. Smith, and M. E. Sale, "A genetic algorithm-based, hybrid machine learning approach to model selection," *J. Pharmacokinet. Pharmacodyn.*, vol. 33, no. 2, pp. 195–221, 2006.

[52] K. Deb, "An investigation of niche and species formation in genetic function optimization," in *Proc. 3rd Int. Conf. Genet. Algorithms (ICGA)*, 1989, pp. 42–50.

Shaolong Shi (Student Member, IEEE) received the B.Sc. and M.Sc. degrees in control science and engineering from the Harbin Institute of Technology, Harbin, China, in 2014 and 2016, respectively, and the Ph.D. degree in computer science and technology from the Harbin Institute of Technology and the Southern University of Science and Technology, Shenzhen, China, in 2020.

He is currently a Postdoctoral Fellow with the School of Life Science and Technology, University of Electronic Science and Technology of China, Chengdu, China. His research interest includes computing-inspired biosensing with application to cancer detection.

Yifan Chen (Senior Member, IEEE) has held various academic and leadership positions in universities in China, New Zealand, U.K., and Singapore. His current research interests include natural computation-inspired nanobiosensing, molecular communications-inspired nanobiomedicine, electromagnetic medical imaging and sensing for low-cost and lightweight healthcare.

Xin Yao (Fellow, IEEE) received the B.Sc. degree from the University of Science and Technology of China (USTC), Hefei, China, in 1982, the M.Sc. degree from the North China Institute of Computing Technologies, Langfang, China, in 1985, and the Ph.D. degree from USTC in 1990.

He is currently a Chair Professor of Computer Science with the Southern University of Science and Technology, Shenzhen, China, and a part-time Professor of Computer Science with the University of Birmingham, Birmingham, U.K. His major research interests include evolutionary computation, ensemble learning, and their applications to software engineering.

Dr. Yao work won the IEEE Donald G. Fink Prize Paper Award (which was published in Proceedings of the IEEE in 1999) in 2001; the IEEE TRANSACTIONS ON EVOLUTIONARY COMPUTATION Outstanding Paper Awards in 2010, 2016, and 2017; the IEEE TRANSACTIONS ON NEURAL NETWORKS Outstanding Paper Award in 2011; and many other best paper awards at conferences. He received a prestigious Royal Society Wolfson Research Merit Award in 2012, the IEEE CIS Evolutionary Computation Pioneer Award in 2013, and the IEEE Frank Rosenblatt Award in 2020. He was a Distinguished Lecturer of the IEEE Computational Intelligence Society. He was a President of IEEE CIS from 2014 to 2015 and the Editor-in-Chief of IEEE TRANSACTIONS ON EVOLUTIONARY COMPUTATION from 2003 to 2008.